



FeMo-based catalysts for H₂ production by NH₃ decomposition

Barbara Lorenzut, Tiziano Montini*, Manuela Bevilacqua¹, Paolo Fornasiero

Department of Chemical and Pharmaceutical Sciences and ICCOM-CNR Trieste Research Unit, University of Trieste, via L. Giorgieri 1, 34127 Trieste, Italy

ARTICLE INFO

Article history:

Received 3 April 2012

Received in revised form 8 June 2012

Accepted 12 June 2012

Available online 21 June 2012

Keywords:

Hydrogen

Ammonia decomposition

Iron

Molybdenum

Nitrides

ABSTRACT

Active and stable catalysts for ammonia decomposition were obtained by deposition of Fe(5 wt%)-Mo(5 wt%) on commercial stabilized zirconia and modified aluminas. The adopted preparation methodology, combined with a severe reduction treatment, allowed obtaining highly dispersed nanoparticles of Fe–Mo alloy, as revealed by powder XRD. The bimetallic catalysts demonstrated a higher activity with respect to the monometallic ones with the same metal loading (10 wt%). The best performances were obtained for a bimetallic Fe₅Mo₅/La₂O₃-modified Al₂O₃ sample. During ammonia decomposition reaction, the Fe–Mo alloy was progressively converted into a mixture of Fe/Mo nitrides, while good catalytic activity was maintained. The performances of the present catalysts well fit with the requirements of catalysts for application in ammonia-fueled SOFCs or for internal combustion engines.

© 2012 Elsevier B.V. All rights reserved.

1. Introduction

The growing concern for both environmental pollution and the irreversible decline of fossil fuels reservoirs is pushing the attention of decision makers and scientists towards the identification of non conventional fuels [1,2]. Hydrogen, in combination with fuel cells (FC), is generally considered a promising option to ultimately solve pollution problems in urban areas. However, the still unresolved problem of large scale and sustainable hydrogen production, the open question on its distribution and storage infrastructures, the still serious limitations of today's PEM-FCs, and the enormous cost for all these infrastructures have stimulated the attention to alternative and/or complementary solutions. In this context, increasing research works are dedicated to the evaluation of ammonia (NH₃) as possible alternative energy vector [3]. In fact, it can be used for the production of C-free H₂ or as an ultimate fuel in SOFC [4–6] and in internal combustion engines (ICEs) [7,8]. In this latter case, only small modification of the conventional spark ignition engines are needed. However, due to its high autoignition temperature (651 °C), ammonia needs a flame accelerator, such as hydrogen, in order to burn efficiently. Therefore, also in the case of ICEs, ammonia must be partially decomposed to H₂/N₂ mixture [8].

Ru-based materials are the most active catalysts for ammonia decomposition reaction [9–15]. However, the limited availability of

this noble metal and its high cost force the development of alternative catalysts comprising less expensive and largely available non precious metals. In this context, Zhang et al. [16] reported high ammonia conversion (60%) at 500 °C (GHSV = 30,000 mL g^{−1} h^{−1}) using Ni (~45 wt%) supported on La-doped Al₂O₃ synthesized by co-precipitation. The addition of CeO₂ to Ni/Al₂O₃ led to an improvement of both the activity and the stability of catalyst [17]. Fe-based catalysts comprising different metal oxides or carbon nanotubes as supports were reported to be active both in the ammonia synthesis and in the ammonia decomposition reaction [18–21]. Choi [22] showed that early transition metal carbides and nitrides are active in ammonia decomposition, with catalytic properties similar to those of platinum-group metals. Remarkably, while vanadium films presented poor ammonia decomposition capability, their activity strongly enhanced after bulk nitridation [23]. Consistently nitridation or carburization of the bulk metals (vanadium and molybdenum) was indicated as a successful methodology to the enhance catalytic activity of bare base metals [24]. Recently, zirconium oxynitride were found to be active in ammonia decomposition [25].

Starting from the consideration that both Fe and Mo are active in ammonia decomposition and that the same metals are involved in various steps of the biological processes of N₂ fixation as NH₄⁺ [26,27], we studied the development of bimetallic Fe_xMo_y-based heterogeneous catalysts for ammonia decomposition. The structural/morphological characteristics of Fe_xMo_y active phases deposited over different supports were investigated and correlated with the performances in ammonia decomposition. To evaluate synergistic effects between the two metals, monometallic catalysts were used as reference materials.

* Corresponding author. Tel.: +39 040 558 3981; fax: +39 040 558 3903.

E-mail address: tmontini@units.it (T. Montini).

¹ Present address: Institute of Chemistry of OrganoMetallic Compounds, ICCOM-CNR, Via Madonna del Piano 10, 50019 Sesto Fiorentino (FI), Italy.

2. Experimental

2.1. Synthesis of the catalysts

Various commercial stabilized ZrO₂ (MEL Chemicals, UK) and modified Al₂O₃ were used as supports for Mo and Fe.

Commercial ZrO₂ doped with Y, La or Ce (Mel Chemicals, UK, denoted as YSZ, LSZ and CSZ, respectively) were chosen for their high thermal stability and with the aim to allow an easier scale-up production in view of an industrial application. Commercial Al₂O₃ (SASOL, Germany) was modified with 10 wt% of La₂O₃ by impregnation with La(NO₃)₃·9H₂O dissolved in ethanol (La–Al₂O₃) or with a 10 wt% of Ce_{0.6}Zr_{0.4}O₂ by impregnation with an aqueous citrate-gel comprising Ce and Zr (CZ–Al₂O₃) [28]. The presence of dopants and stabilizers has the double role of increasing the thermal stability and decrease the acidity of the bare supports. This latter aspect is important as the NH₃ decomposition reaction is favored over basic supports [10,12,29].

Before impregnation with Fe and Mo precursors, the supports were calcined at 900 °C for 5 h to stabilize their texture and structure.

The procedure for the preparation of the catalysts was designed in order to optimize the metal dispersion and to maximize the formation of an alloy between Fe and Mo. This can be done by careful co-deposition of Fe and Mo precursors onto the support. Therefore it is essential to select both suitable metal precursors and solvents that guarantee total solubility and stability of the solution during the impregnation of the support. The commonly used inorganic precursors Fe(NO₃)₃·9H₂O and (NH₄)₂Mo₇O₂₄·4H₂O cannot be used in aqueous solution because of the fast precipitation of Fe–Mo mixed oxides [30]. In a preliminary study, we prepared Fe₁₀Mo₁₀/YSZ catalysts by consecutive impregnation of the support changing the order of the metal deposition: first Fe(NO₃)₃·9H₂O and (NH₄)₂Mo₇O₂₄·4H₂O after an intermediate calcination or first (NH₄)₂Mo₇O₂₄·4H₂O and Fe(NO₃)₃·9H₂O after an intermediate calcination. In both the cases, the final activity in NH₃ decomposition was poor and very far from the requirements for practical applications. Subsequently, acetylacetonates Fe(acac)₃ and MoO₂(acac)₂ were identified as optimal precursors, since they are both soluble in acetone and no reaction between them was observed.

Therefore, the metal loaded samples were prepared by co-impregnation using bis (acetylacetonate) dioxomolybdenum (VI) MoO₂(acac)₂ (>99.9% Aldrich) and iron(III) acetylacetonate Fe(acac)₃ (>99.9% Aldrich) as metal precursors. Briefly, appropriate amounts of the precursors were dissolved in acetone under vigorous stirring for 1 h. Meanwhile, the support (doped ZrO₂ or Al₂O₃) was suspended in acetone. Subsequently, the solution of the metal precursors was added to the suspension containing the support under vigorous stirring. The final suspension was stirred for 1 h and then the solvent was evaporated under vacuum. The solid residue was dried overnight at 120 °C in air. The material was further calcined in a static oven at 400 °C for 5 h (heating rate 1 °C min^{−1}, cooling rate 4.5 °C min^{−1}).

The obtained materials (Table 1) are designated as Fe_xMo_y/Support, where x and y represent the iron and molybdenum loading (wt%).

2.2. Catalysts characterization

Characterization of the catalysts was performed in terms of textural properties (by means of N₂ physisorption at the liquid nitrogen temperature), structural properties (by means of powder X-ray diffraction – XRD and Raman spectroscopy) and redox properties (by means of temperature programmed reduction – TPR).

Table 1

Fe/Mo based catalysts composition.

Sample	Fe (wt%)	Mo (wt%)	Support composition (mol%)
Fe ₁₀ /YSZ	10%	–	Y ₂ O ₃ (8%)–ZrO ₂
Mo ₁₀ /YSZ	–	10%	Y ₂ O ₃ (8%)–ZrO ₂
Fe ₁₀ Mo ₁₀ /YSZ	10%	10%	Y ₂ O ₃ (8%)–ZrO ₂
Fe ₅ Mo ₅ /YSZ	5%	5%	Y ₂ O ₃ (8%)–ZrO ₂
Fe ₅ Mo ₅ /LSZ	5%	5%	La ₂ O ₃ (10%)–ZrO ₂
Fe ₅ Mo ₅ /CSZ	5%	5%	CeO ₂ (15%)–ZrO ₂
Fe ₅ Mo ₅ /La–Al ₂ O ₃	5%	5%	La ₂ O ₃ (10%)–Al ₂ O ₃
Fe ₅ Mo ₅ /CZ–Al ₂ O ₃	5%	5%	Ce _{0.6} Zr _{0.4} O ₂ (10%)–Al ₂ O ₃

N₂ physisorption isotherms were collected using a Micromeritics ASAP 2020 on 100–200 mg of each sample, after degas them at 350 °C overnight.

TPR experiments were performed in a home-made apparatus using ~40 mg of each sample. After cleaning by O₂ pulsing in an Ar flow at 400 °C for 1 h, the gas flow was switched to H₂ (5%)/Ar (25 mL min^{−1}) and the temperature was increased with a rate of 10 °C min^{−1}. H₂ consumption was measured by a thermal conductivity detector (TCD).

Powder XRD patterns were collected in the 10–100° range by means of a Philip X'Pert instrument using the Cu Kα radiation. Since storage and XRD measurements were performed without adopting inert atmosphere for storage and transportation of the samples, XRD analyses of the activated and aged catalysts were performed reducing as more as possible the time of their exposition of the samples to air, in order to avoid significant re-oxidation of eventual metallic phases present in the materials. Crystallite sizes (C.S., expressed in nm) were calculated according the following Sherrer's equation:

$$C.S. = \frac{K\lambda}{\beta \cos \theta}$$

where $K=0.9$, λ is the X-ray wavelength (0.1541 nm), θ is Bragg angle of the considered reflection and β is the line broadening at half the maximum intensity (FWHM). β is calculated as follow:

$$\beta = \sqrt{B_{obs}^2 - B_{inst}^2}$$

where B_{obs} is the FWHM measured for the considered reflection and B_{inst} is the instrumental FWHM, measured considering the XRD pattern of a standard material (with very large crystallites) on a reflection as close as possible to the experimental reflection of the sample.

Raman spectra were recorded using a Renishaw Invia microspectrometer, equipped with a He–Ne NIR laser line (633 nm) and a 50× objective. Raman measurements were carried out with a laser power of 10 mW at the sample and a collection time of 20 s.

2.3. Catalytic activity

The apparatus used to study the catalytic activity and the analytical procedure adopted to evaluate the composition of the gaseous mixture at the exit of the reactor were previously described in Ref. [15]. Catalytic activity experiments were performed using both pure ammonia (transistor grade purity) or technical ammonia (that contains approximately 3000 ppm of H₂O, 50 ppm of O₂ and 10 ppm of hydrocarbons). The mass of catalysts and the gas flow rates were adjusted in order to test the samples under GHSV = 46,000 mL g^{−1} h^{−1} (67 mg of catalyst, diluted in 133 mg of inert α-Al₂O₃, and 51.4 mL min^{−1} of NH₃). Samples were diluted with α-Al₂O₃ to lengthen the catalytic bed and improve thermal uniformity along it.

The calcined materials were activated by reduction in H_2 flow (35 mL min^{-1}) at 800°C for 2 h before the ammonia decomposition experiments. After purging with Ar flow (35 mL min^{-1}) for 30 min, the temperature was decreased to 400°C before NH_3 was introduced into the reactor. The catalytic activity was evaluated every 50°C from 400 to 800°C . At least 5 activity cycles were applied on the same catalyst to verify its stability after reaction at high temperature. In addition, steady state stability test were performed, after activation by H_2 reduction at 800°C , at 650°C analyzing the reaction products every hour.

3. Results and discussion

3.1. Catalysts characterization

3.1.1. Temperature programmed reduction (TPR) and Raman investigations

The reducibility of the samples was investigated by means of temperature programmed reduction (TPR) (Fig. 1). As a general feature, the samples present various reduction processes, operative at low ($T < 600^\circ\text{C}$) and high temperature ($T > 600^\circ\text{C}$).

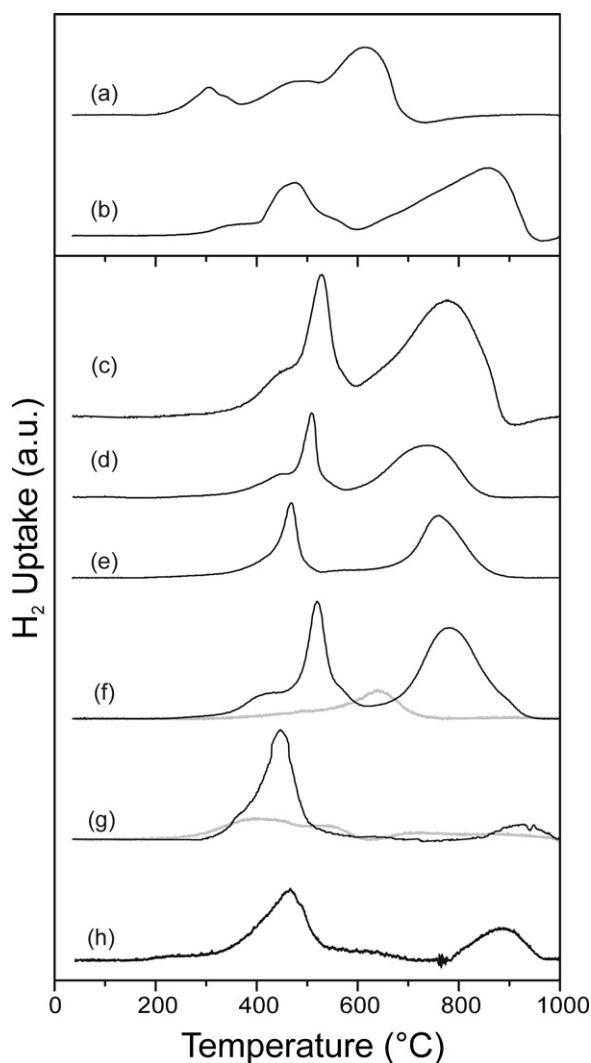
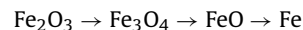


Fig. 1. TPR profiles of calcined samples after a standard cleaning procedures: $\text{Fe}_{10}/\text{YSZ}$ (a), $\text{Mo}_{10}/\text{YSZ}$ (b), $\text{Fe}_{10}\text{Mo}_{10}/\text{YSZ}$ (c), $\text{Fe}_5\text{Mo}_5/\text{YSZ}$ (d), $\text{Fe}_5\text{Mo}_5/\text{LSZ}$ (e), $\text{Fe}_5\text{Mo}_5/\text{CSZ}$ (f), $\text{Fe}_5\text{Mo}_5/\text{CZ}-\text{Al}_2\text{O}_3$ (g) and $\text{Fe}_5\text{Mo}_5/\text{La}-\text{Al}_2\text{O}_3$ (h). Gray lines present the TPR profile of the corresponding supports, when they contain Ce.

The reductions of Fe_2O_3 and MoO_3 can be multi-step processes, accordingly to the following transformations:



Consistently, the TPR profile of Fe_2O_3 and MoO_3 are characterized by multiple H_2 consumption peaks, as previously reported in the literature. Brown et al. [31] studied the reducibility of bulk iron oxide, showing that the reduction of Fe_2O_3 proceeds in three steps, the first of which is its reduction to Fe_3O_4 . In the case of molybdenum oxide supported on $\gamma\text{-Al}_2\text{O}_3$, the reducibility of MoO_3 was correlated to the surface coverage of the support [32].

The TPR profile of $\text{Fe}(10\%)/\text{YSZ}$ sample (Fig. 1, trace a) is characterized by three different contributes (300 , 450 and 620°C) in agreement with the presence of Fe_2O_3 . The TPR profile for $\text{Mo}(10\%)/\text{YSZ}$ sample (Fig. 1, trace b) evidenced an hydrogen uptake below 600°C and a high temperature contribute (about 900°C), suggesting the presence of MoO_3 entities.

The nature of the support and the presence of both the active components in the co-doped systems affect the TPR profiles. Multiple reduction peaks are observed in the profiles (Fig. 1, traces c–h), suggesting that Fe and Mo are present in their higher oxidation states – Fe(III) and Mo(VI). The reduction processes operative below 600°C are shifted to higher temperature with respect to the corresponding processes in the monometallic systems. On the contrary, the reduction processes operative above 600°C are promoted, with the peak temperatures comprised in between those observed in the case of the monometallic samples. Notably, Fe_xMo_y species deposited on different supports show rather similar TPR profiles, indicating that the nature of the support has a limited effect on the reducibility of the Fe_xMo_y species. Vice versa, marked difference are observed comparing the TPR profiles of $\text{Fe}_x\text{Mo}_y/\text{supports}$ (Fig. 1, traces c–h) with those of the monometallic $\text{Fe}_{10}/\text{YSZ}$ and $\text{Mo}_{10}/\text{YSZ}$ (Fig. 1, traces a and b). This suggest the existence of some interactions between the two reducible species – Fe(III) and Mo(VI). In this context, the formation of Fe–Mo mixed oxides must be considered, although the mild calcination temperature (400°C) do not allow their detection in the as prepared samples by XRD (see below). In fact, many iron–molybdenum mixed oxides are reported in the literature, such as $\text{Fe}_2\text{Mo}_3\text{O}_8$, $\text{Fe}_2(\text{MoO}_4)_3$, Fe_2MoO_4 and FeMoO_4 [33]. The reduction properties of Fe–Mo mixed oxides were widely investigated with the aim to understand the formation of Fe–Mo alloys [34–37].

In order to further investigate this point, surface characterization was performed by means of Raman spectroscopy. Fig. 2 shows Raman spectra recorded for $\text{Fe}_{10}\text{Mo}_{10}/\text{YSZ}$ calcined at 400°C , where the high concentration of metals allows a better characterization. The sample shows the presence of various Raman signals in the range $100\text{--}1100 \text{ cm}^{-1}$. Notably, since the adopted micro-Raman allows to sampling different zone of the sample, a significant number of Raman spectra were collected to assess for the homogeneity of the surface distribution of Fe–Mo species. Common spectra recorded on the $\text{Fe}_{10}\text{Mo}_{10}/\text{YSZ}$ sample (gray lines in Fig. 2) present main Raman peaks located at 970 , 786 and 351 cm^{-1} , with a small peak at 638 cm^{-1} . This last signal can be assigned to tetragonal YSZ [38,39] and its low intensity suggests that the surface of the support is efficiently covered by Fe–Mo oxides. Intense Raman bands at 352 , 781 and 972 cm^{-1} are reported for bulk $\text{Fe}_2(\text{MoO}_4)_3$ [40,41]. These values well fit with the position of Raman peaks in our calcined $\text{Fe}_{10}\text{Mo}_{10}/\text{YSZ}$ sample and confirm the formation of mixed Fe–Mo oxides. Among the various spectra recorded, important differences were observed in two cases over 30 spectra (black lines in Fig. 2). One of these spectra present intense bands that resemble those of $\text{Fe}_2(\text{MoO}_4)_3$, indicating that an agglomerate made by Fe–Mo mixed oxides is present in this area. The other spectrum shows, together

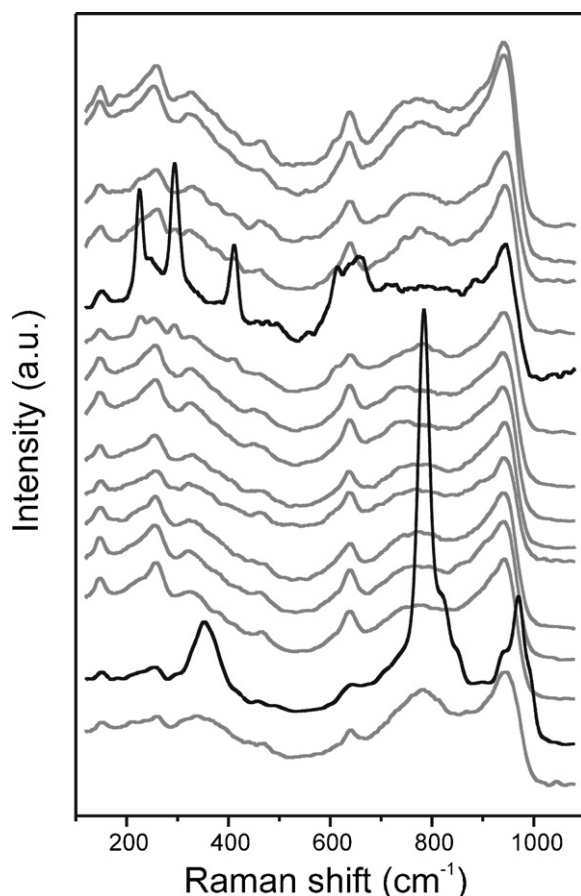


Fig. 2. Raman spectra of the $\text{Fe}_{10}\text{Mo}_{10}/\text{YSZ}$ calcined at 400°C for 5 h acquired on different portion of the sample.

with the peaks related to YSZ and $\text{Fe}_2(\text{MoO}_4)_3$, four Raman peaks centered at 225, 294, 412 cm^{-1} and a small peak at 613 cm^{-1} . This feature is compatible with the presence of Fe_2O_3 as it shows Raman peaks at 300, 410 and 610 cm^{-1} [42]. Notably, peaks centered at 287, 668, 821 and 998 cm^{-1} are reported as the most intense signals for bulk MoO_3 and for MoO_3 supported on ZrO_2 [43,44]. All these results suggest that some Fe_2O_3 is present together with the main $\text{Fe}_2(\text{MoO}_4)_3$ phase. Notably, the Fe/Mo molar in $\text{Fe}_2(\text{MoO}_4)_3$ (Fe/Mo = 0.67) is significantly lower than that expected from the synthesis conditions (Fe/Mo = 1.72), further corroborating the evidences on the presence of segregated Fe_2O_3 .

The formation of $\text{Fe}_2(\text{MoO}_4)_3$ and of some Fe_2O_3 after calcination of the impregnated materials evidenced by Raman spectroscopy is consistent with the multiple reduction processes observed during TPR experiments (Fig. 1).

The shift towards higher temperatures of the reduction peaks in the sample $\text{Fe}_{10}\text{Mo}_{10}/\text{YSZ}$ with respect to $\text{Fe}_5\text{Mo}_5/\text{YSZ}$ could be explained with the different aggregation of oxide nanoparticles correlated with the higher metal loading and/or to a different strength of their interaction with the support. Finally, the total H_2 consumption for the $\text{Fe}_5\text{Mo}_5/\text{CSZ}$ sample is higher than of the other samples with the same Fe/Mo amounts due to the contribution of the CSZ reduction. In fact, the TPR profile of the CSZ support shows a single reduction process in the temperature range 400–700 $^\circ\text{C}$. Therefore, the reduction of the support superimposes with that of the active phase precursors deposited by impregnation. Notably, the reduction of the CSZ support is influenced by the presence of the Fe/Mo phase(s), since the maximum of the reduction rate of the pure support corresponds to a relative minimum of the TPR profile of $\text{Fe}_5\text{Mo}_5/\text{CSZ}$ sample.

In order to fully reduce the metal species before the reactivity tests, an in situ pretreatment in H_2 flow (35 mL min^{-1}) at 800°C for 2 h was applied to all the materials.

3.1.2. Textural characterization

The texture of the catalysts was analyzed by means of N_2 physisorption (Table 2). All the samples present a type IV isotherm with hysteresis loop typical of mesoporous materials. The t -plot analysis indicates that the microporous volume is negligible. The BJH analysis reveals that the materials have a pore distribution centered between 10 and 30 nm. The catalysts prepared using modified- Al_2O_3 as support show higher surface area and larger pore volume with respect to those prepared using doped- ZrO_2 as support (90–95 $\text{m}^2 \text{g}^{-1}$ for Al_2O_3 -based materials versus 30–60 $\text{m}^2 \text{g}^{-1}$ for the ZrO_2 -based materials). The materials calcined after impregnation with Fe/Mo precursors shows a slightly lower surface area and pore volume with respect to the corresponding bare supports, as a result of the partial pore blocking or covering of the internal surface of the pores. Finally, the reduction applied to the samples, as activation pre-treatment, do not affect significantly the textural characteristics of the samples. The observed small increase of the average pore size after activation is a consequence of the collapse or occlusion of the smaller pores during the reduction.

3.1.3. Powder X-ray diffraction (XRD)

Powder X-ray diffraction (XRD) was used to study the evolution of the active phase (comprising Fe and Mo) after different treatments.

XRD patterns of the calcined samples present only the reflections of the supports. The commercial zirconias, doped with yttrium (YSZ), lanthanum (LSZ) or cerium (CSZ) are homogeneous solid solutions with a tetragonal structure (space group $P4_2/nmc$), accordingly with the amount of the dopant cations. The cell parameters are in line with those calculated for the corresponding solid solutions and considering the Vegard law. A mean crystallite size of 24, 20 and 21 nm was calculated for YSZ, LSZ and CSZ respectively.

In the case of Al_2O_3 -based supports, the broad reflections of the transitional Al_2O_3 complicate phase attribution. Nevertheless, the reflections of the CZ phase (in $\text{Fe}_5\text{Mo}_5/\text{CZ}-\text{Al}_2\text{O}_3$) and of LaAlO_3 (in $\text{Fe}_5\text{Mo}_5/\text{La}-\text{Al}_2\text{O}_3$) can be clearly distinguished. A mean crystallite size of 6 and 14 nm was calculated for the CZ and LaAlO_3 phases, respectively. Notably, no reflection related to Fe and/or Mo-containing species were observed in the calcined samples. This result is consistent with the low temperature calcination treatment (400°C), which leads to well dispersed Fe and Mo oxides over the high surface area supports.

Fig. 3 presents the XRD patterns of the catalysts prepared using doped- ZrO_2 as supports after activation treatment by H_2 reduction at 800°C . The crystallite size of the supports are almost unaffected by the activation treatment (Table 3). This is consistent with the fact that they were preconditioned at a higher temperature (calcination at 900°C). The most intense reflections of the metallic Fe (JCPDS 06-0696) and Mo (JCPDS 04-0809) were observed in the XRD patterns of $\text{Fe}_{10}/\text{YSZ}$ and $\text{Mo}_{10}/\text{YSZ}$, respectively (Fig. 3). The (1 1 0) reflection of Fe is present in all bimetallic Fe_xMo_y -based samples. This reflection is particularly broad in the $\text{Fe}_5\text{Mo}_5/\text{LSZ}$ sample indicating the formation of very small Fe crystallites. The main reflection of metallic Mo is present only in the XRD pattern of the $\text{Fe}_{10}\text{Mo}_{10}/\text{YSZ}$ sample, thanks to the high metal loading. A very broad signal is present between the main reflections of metallic Fe and Mo (Fig. 3, right part). This broad signal can be attributable to the (1 1 0) reflection of a Fe–Mo alloy with a very small crystallite size (~ 3 nm), although the exact composition cannot be precisely assigned. In fact, the Fe–Mo phase diagram [34] shows the presence of various stable Fe–Mo alloys.

Table 2

Catalysts textural properties after calcinations and standard activation pre-treatment.

Samples	Calcined ^a			Activated ^b		
	SSA ^c (m ² g ⁻¹)	d _M ^d (nm)	CPV ^e (mL g ⁻¹)	SSA ^c (m ² g ⁻¹)	d _M ^d (nm)	CPV ^e (mL g ⁻¹)
YSZ	29	18/37	0.19			
LSZ	59	11/38	0.26			
CSZ	34	16/57	0.17			
Al ₂ O ₃	102	29	1.01			
CZ–Al ₂ O ₃	95	39	0.79			
La–Al ₂ O ₃	90	28	0.91			
Fe ₁₀ /YSZ	27	14	0.15	17	22/36	0.15
Mo ₁₀ /YSZ	25	19/37	0.17	13	18/37	0.14
Fe ₁₀ Mo ₁₀ /YSZ	27	9/13	0.12	23	18/30	0.12
Fe ₅ Mo ₅ /YSZ	30	11/38	0.14	26	18/37	0.16
Fe ₅ Mo ₅ /LSZ	52	10/38	0.21	51	12/40	0.22
Fe ₅ Mo ₅ /CSZ	30	8/56	0.13	29	10/56	0.15
Fe ₅ Mo ₅ /CZ–Al ₂ O ₃	89	27	0.63	83	39	0.64
Fe ₅ Mo ₅ /La–Al ₂ O ₃	92	28	0.74	86	28	0.76

^a Bare supports calcined at 900 °C for 5 h; Fe–Mo-based catalysts calcined in air at 400 °C for 5 h after impregnation.^b After reduction in H₂ flow at 800 °C for 2 h.^c Specific surface area.^d Maxima of the pore distribution calculated by BJH analysis of the desorption branch of the N₂ isotherm.^e Cumulative pore volume.

Fig. 4 shows the XRD patterns of the reduced Fe₅Mo₅/CZ–Al₂O₃ and Fe₅Mo₅/La–Al₂O₃ in comparison with those of the correspondent supports. The XRD analysis of these samples is rather complex due to the co-existence of many different phases. In Fig. 4, the reflection of Ce_{0.6}Zr_{0.4}O₂, LaAlO₃ and Fe are evidenced, since these are the only phases clearly identified. In addition to the presence of a significant amounts of amorphous material, the incomplete stabilization of transitional aluminas does not allow univocal phase

attribution of the other reflections as well as Rietveld refinement of the overall patterns. However, an analysis of the XRD patterns can be performed by fitting the patterns with an adequate number of pseudo-Voigt functions, allowing to isolate the (1 1 0) reflection of metallic Fe. A crystallite size of ~12 nm was consistently calculated. No reflections clearly attributable to phases containing Mo (metallic or Fe–Mo alloys) could be unambiguously identified due to overlapping with reflections of transitional aluminas.

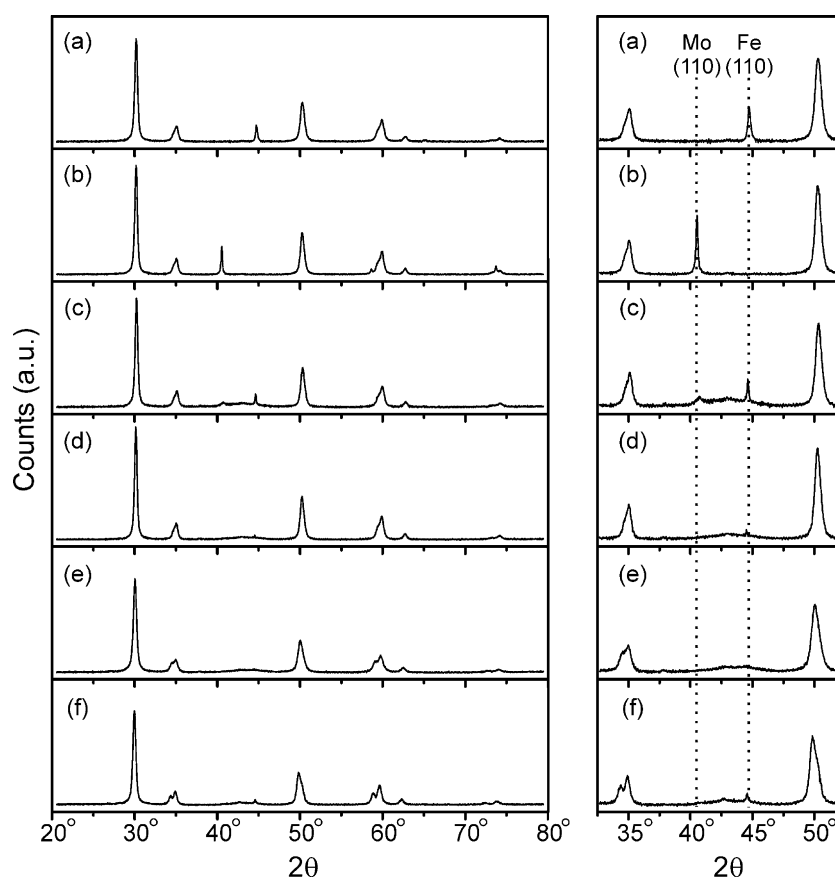


Fig. 3. XRD patterns of the samples after standard activation (reduction in H₂ at 800 °C for 2 h): Fe₁₀/YSZ (a), Mo₁₀/YSZ (b), Fe₁₀Mo₁₀/YSZ (c), Fe₅Mo₅/YSZ (d), Fe₅Mo₅/LSZ (e) and Fe₅Mo₅/CSZ (f).

Table 3
Phase composition and crystallite size of reduced samples.

Sample	Phase	Crystallite size (nm)
Fe ₁₀ /YSZ	YSZ	22
	Fe	42
Mo ₁₀ /YSZ	YSZ	24
	Mo	57
	YSZ	24
Fe ₁₀ Mo ₁₀ /YSZ	Fe	63
	Fe–Mo Alloy	3
	Mo	18
	YSZ	25
Fe ₅ Mo ₅ /YSZ	Fe	145
	Fe–Mo Alloy	3
	LSZ	20
	CSZ	21
Fe ₅ Mo ₅ /LSZ	Fe	3
	Fe–Mo Alloy	4
	CSZ	21
	Fe	53
Fe ₅ Mo ₅ /CSZ	Fe	3
	Fe–Mo Alloy	3
	Fe	12
Fe ₅ Mo ₅ /CZ–Al ₂ O ₃	CZ	6
	Fe	12
Fe ₅ Mo ₅ /La–Al ₂ O ₃	Fe	12
	LaAlO ₃	14

3.2. Catalytic activity

3.2.1. NH₃ decomposition results

Catalytic tests were performed under atmospheric pressure and using pure NH₃. High GHSV (46,000 mL g^{−1} h^{−1}) experiments were used to simulate working conditions of internal combustion engine based on ammonia and of NH₃-SOFC. In the first case, since only a quite low H₂ concentration is needed to optimize ammonia combustion, the attention is focused on low NH₃ conversion, that means study the activity at medium-low temperature. Vice versa, in the case of SOFC, the ammonia conversion must be high bringing the attention to high temperature performances. All the catalysts were subjected to many consecutive catalytic cycles, increasing the reactor temperature up to 700 °C.

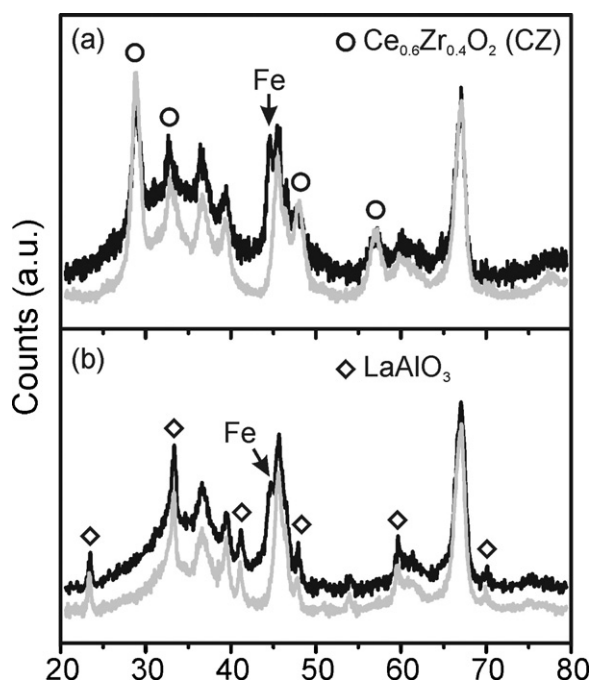


Fig. 4. XRD patterns of the samples after standard activation: Fe₅Mo₅/CZ–Al₂O₃ (a) and Fe₅Mo₅/La–Al₂O₃ (b). The gray lines show the XRD patterns of the correspondent supports.

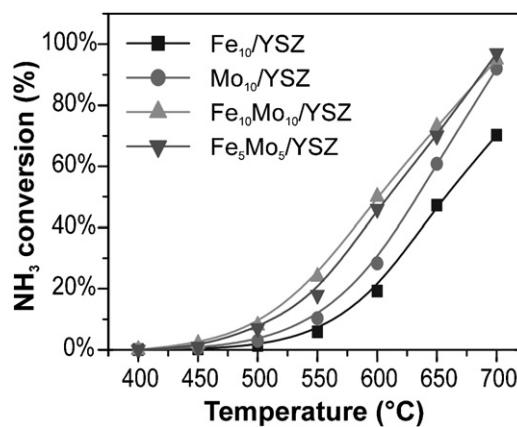


Fig. 5. NH₃ decomposition at GHSV = 46,000 mL g^{−1} h^{−1} over different Fe/Mo catalysts supported on YSZ pre-reduced at 800 °C for 2 h.

Blank experiments performed using α -Al₂O₃ alone or the bare supports diluted with α -Al₂O₃ demonstrated negligible NH₃ conversion, even at 700 °C.

Fig. 5 shows the conversion of NH₃ on reduced Fe/Mo-based catalysts supported on YSZ. NH₃ conversion starts around 400 °C, increasing progressively with the catalyst temperature. For Fe₁₀/YSZ catalyst, a maximum NH₃ conversion of ~70% is obtained at 700 °C, while Mo₁₀/YSZ reaches the complete conversion to H₂/N₂ mixture. The bimetallic Fe₁₀Mo₁₀/YSZ and Fe₅Mo₅/YSZ catalysts also reach the complete conversion of ammonia at 700 °C, while the most important differences with respect to the monometallic samples is observed in the intermediate temperature range (500–600 °C), presenting a higher H₂ content in the gas mixture. In fact, at 550 °C, the volume percentage of H₂ in the gas stream coming from the reactor was 29.0 vol% and 21.3 vol% when Fe₁₀Mo₁₀/YSZ and Fe₅Mo₅/YSZ were used, corresponding to an NH₃ conversion of 24.1% and 16.2%, respectively. On the other hand, only 8.3 vol% and 14.0 vol% of H₂ in the gas stream were obtained using the monometallic Fe₁₀/YSZ and Mo₁₀/YSZ, corresponding to NH₃ conversion of 5.9% and 10.3%, respectively. This result is relevant in view of the possible use of ammonia in ICE. In fact, the H₂ needed to co-feed the engine could be produced on-board using a decomposition reactor conveniently heated by the engine themselves. In this case, the operative temperature of the decomposition reactor should lie around 500–550 °C. Notably, the amount of H₂ necessary to efficiently maintain ammonia combustion is quite low, around 5–10 vol%. From Fig. 5, it is possible to appreciate that bimetallic Fe₁₀Mo₁₀/YSZ and Fe₅Mo₅/YSZ decompose enough ammonia to reach the desired amount of 10 vol% of H₂ at 489 and 502 °C, respectively. Vice versa, the monometallic Fe₁₀/YSZ and Mo₁₀/YSZ, gain the same performances at significantly higher temperature, 552 and 526 °C, respectively. The higher activity of Fe₁₀Mo₁₀/YSZ with respect to the monometallic Fe₁₀/YSZ and Mo₁₀/YSZ and to the bimetallic Fe₅Mo₅/YSZ can be easily related with the effective higher loading of the active phases. Remarkably, the NH₃ conversion obtained at 550 °C using Fe₁₀Mo₁₀/YSZ (24.1%) is higher than the sum of the conversions obtained using the two monometallic catalysts (10.3% + 5.9% = 16.2%). This fact can be explained considering the high dispersion of the two metals in Fe₁₀Mo₁₀/YSZ with the formation of Fe–Mo alloy, as evidenced by XRD analysis. Similarly, the high dispersion of the alloyed active phase can justify the higher activity of Fe₅Mo₅/YSZ with respect to the monometallic catalysts with the same metal loading. Notably, hydrogen production from NH₃ decomposition was predicted to be easier on nanosized Fe clusters with respect to large Fe surfaces [45].

Because of the similar activities of Fe₁₀Mo₁₀/YSZ and Fe₅Mo₅/YSZ, we decided to investigate the effect of the support on

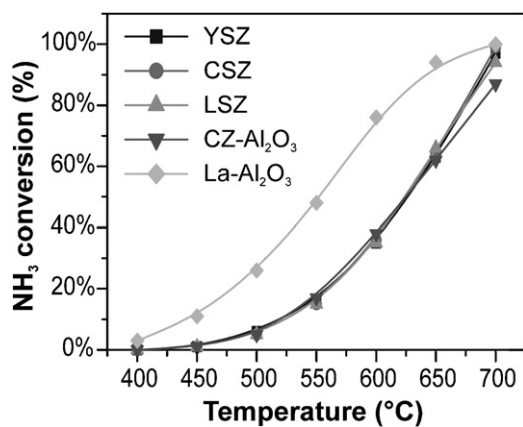


Fig. 6. NH_3 decomposition at GHSV = $46,000 \text{ mL g}^{-1} \text{ h}^{-1}$ over Fe_5Mo_5 -based catalysts deposited on different supports after pre-reduction at 800°C for 2 h.

the catalytic activity of Fe_5Mo_5 -based catalysts. A series of commercial doped ZrO_2 , with different dopant ions but with comparable surface area, were used. Two more samples with high surface area were prepared using modified Al_2O_3 .

The results of catalytic activity experiments performed with Fe_5Mo_5 -based catalysts are presented in Fig. 6 in terms of NH_3 conversion. Almost identical catalytic performances were observed among the Fe_5Mo_5 on doped ZrO_2 samples. This result is consistent with the small differences between the investigated Y, La and Ce doped zirconia based materials. In fact, the relatively small dopant loadings affect marginally the acid/basic properties of the support. In addition, minor differences were observed in the dispersion of the Fe_5Mo_5 active phase (Table 3). Different is the case of the high surface area modified- Al_2O_3 based catalysts. In fact, while the activity of the $\text{Fe}_5\text{Mo}_5/\text{CZ-Al}_2\text{O}_3$ is comparable with that of the doped- ZrO_2 based samples, a significant improvement is observed in the case of $\text{Fe}_5\text{Mo}_5/\text{La-Al}_2\text{O}_3$. The similar activity observed for the $\text{Fe}_5\text{Mo}_5/\text{CZ-Al}_2\text{O}_3$ and the $\text{Fe}_5\text{Mo}_5/\text{doped zirconias}$, despite the differences in surface area (Table 2) and therefore in the expected metal dispersion, suggests the coexistence of different contributions to the final performances, the understanding of which would require further and more sophisticated investigation techniques. The different basicity of the support contributes to the final activity, but the dispersion of the metal phase is also of paramount importance. The presence of small amount of La, Ce or Y on the doped zirconia leads to extremely different Fe particles, 3, 53 and 145 nm, respectively (Table 3) while the Fe–Mo alloy has rather similar crystallite size for the three systems. This would suggest an important role of the highly dispersed Fe–Mo alloy as catalyst or catalyst precursor. Unfortunately, the complexity of the structure of the alumina based materials precludes an accurate evaluation of the presence of Fe–Mo alloy, even if we can expect to be present. The positive effect of the use of supports with basic properties for the NH_3 decomposition activity was clearly demonstrated for both Ru and Fe based catalysts [10,12,29]. Notably, due to its higher activity, $\text{Fe}_5\text{Mo}_5/\text{La-Al}_2\text{O}_3$ reaches an H_2 content of 10 vol% at $\sim 425^\circ\text{C}$, a temperature which is remarkably lower with respect to all the other materials.

Various consecutive NH_3 decomposition experiments were performed to verify the stability of the activity of the catalyst. As an example, Fig. 7 shows the case of $\text{Fe}_5\text{Mo}_5/\text{YSZ}$. No appreciable shift in the light-off temperature was observed indicating excellent thermal stability of the present systems. Moreover, the stability of the catalytic activity under NH_3 decomposition were evaluated under steady-state conditions at 650°C , evidencing constant NH_3 conversion for at least 120 h. Finally, to investigate more realistic conditions, reactivity tests were also performed using low grade

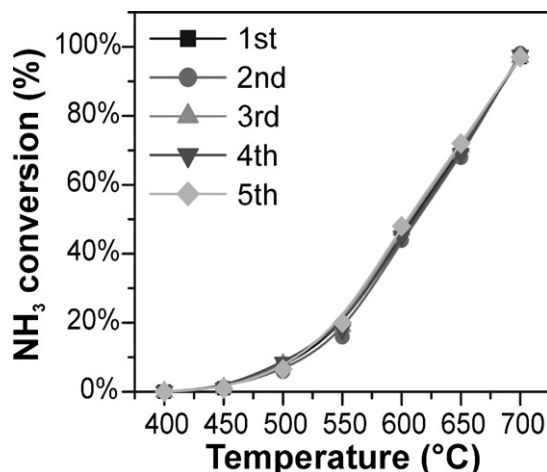


Fig. 7. Consecutive NH_3 decomposition cycles at GHSV = $46,000 \text{ mL g}^{-1} \text{ h}^{-1}$ over $\text{Fe}_5\text{Mo}_5/\text{YSZ}$ pre-reduced at 800°C for 2 h.

– technical ammonia. Almost identical activity and stability results were obtained, indicating that the lower purity of the feedstock has a negligible effect of the catalysts' performances.

3.2.2. Characterization of aged catalysts

Although no appreciable deactivation was observed, the structural investigation of the aged catalysts evidenced important modifications of the nature of the active phase already after 5 activity cycles. Once more, it was not possible to obtain clear structural information from the analysis of the XRD patterns of the aged $\text{Fe}_5\text{Mo}_5/\text{CZ-Al}_2\text{O}_3$ and $\text{Fe}_5\text{Mo}_5/\text{La-Al}_2\text{O}_3$ samples due to the co-existence of various transitional aluminas and to the presence of large amounts of amorphous materials. On the other hand, clear information were available for the samples supported on doped- ZrO_2 . Notably, while the aging did not significant modify the textural properties of the catalysts (surface area, pore volume and pore diameter) structural changes of the active phases were observed by means of XRD analysis, although a detailed characterization of the aged samples was possible only in a few cases. Fig. 8 shows the XRD patterns of selected samples aged under NH_3 decomposition conditions, after 5 activity cycles up to 700°C or after prolonged steady state stability tests at 650°C .

The analysis of these patterns highlights the transformation of Fe–Mo alloy into various nitride species, depending on the nature of the support and the aging treatment. The results of Rietveld analysis are summarized in Table 4. Notably, a reliable estimation of phase composition and cell parameters is obtained only for the

Table 4
Phase composition and crystallite size of aged samples.

Sample	Phase	Crystallite size (nm)
$\text{Fe}_{10}\text{Mo}_{10}/\text{YSZ}$	YSZ	24
After stability at 650°C for 120 h	Fe	39
	Fe_4N	49
	$\text{Mo}_{0.82}\text{N}$	23
$\text{Fe}_{10}\text{Mo}_{10}/\text{YSZ}$	YSZ	27
After 5 cycles up to 700°C	$\text{Fe}(\text{Mo})_3\text{N}_{1.24}$	54
	$\text{Mo}_{0.82}\text{N}$	28
$\text{Fe}_5\text{Mo}_5/\text{YSZ}$	YSZ	23
After 5 cycles up to 700°C	$\text{Fe}(\text{Mo})_3\text{N}_{1.24}$	26
	$\text{Mo}_{0.82}\text{N}$	13
$\text{Fe}_5\text{Mo}_5/\text{LSZ}$	LSZ	22
After 5 cycles up to 700°C	$\text{Fe}(\text{Mo})_3\text{N}_{1.24}$	28
	$\text{Mo}_{0.82}\text{N}$	28
$\text{Fe}_5\text{Mo}_5/\text{CSZ}$	CSZ	20
After 5 cycles up to 700°C	Fe	22
	$\text{Mo}_{0.82}\text{N}$	11

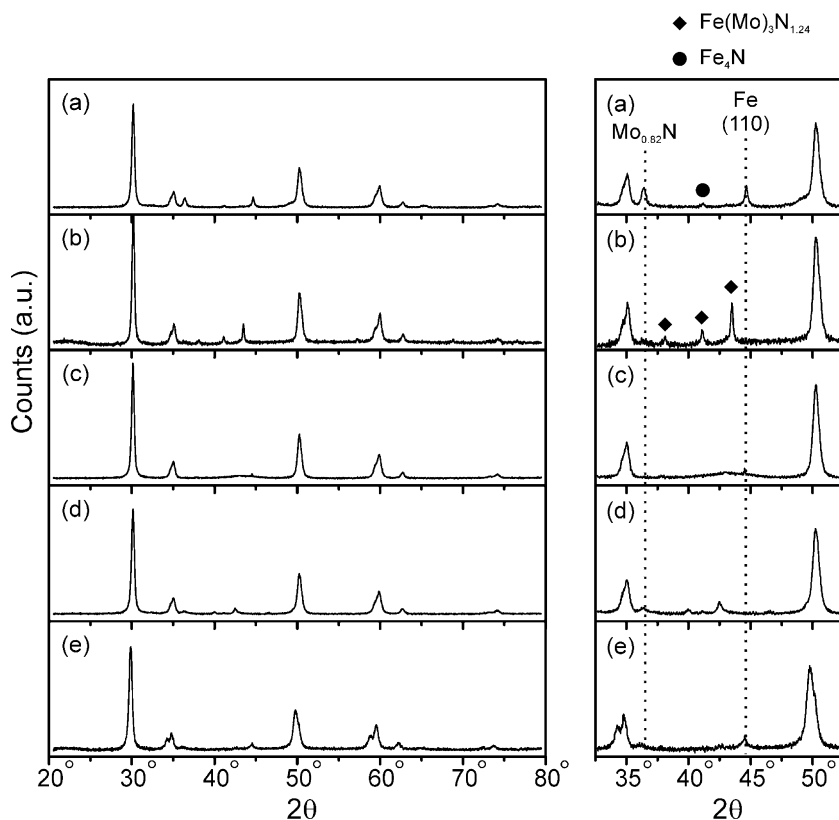


Fig. 8. XRD patterns of the aged samples: $\text{Fe}_{10}\text{Mo}_{10}/\text{YSZ}$ after stability test at 650°C for 120 h (a), $\text{Fe}_{10}\text{Mo}_{10}/\text{YSZ}$ after 5 consecutive cycles up to 700°C (b), $\text{Fe}_5\text{Mo}_5/\text{YSZ}$ after 5 consecutive cycles up to 700°C (c), $\text{Fe}_5\text{Mo}_5/\text{LSZ}$ after 5 consecutive cycles up to 700°C (d) and $\text{Fe}_5\text{Mo}_5/\text{CSZ}$ after 5 consecutive cycles up to 700°C (e).

$\text{Fe}_{10}\text{Mo}_{10}/\text{YSZ}$ sample while, for the catalysts with a lower Fe/Mo content, the results are only qualitative. For $\text{Fe}_{10}\text{Mo}_{10}/\text{YSZ}$, the active phase was completely converted into $\text{Mo}_{0.82}\text{N}$ (JCPDS 75-1006), Fe (JCPDS 06-0696) and Fe_4N (JCPDS 06-0627) after 120 h of reaction at 650°C . The cell parameters for all these phases well agree with their theoretical values, suggesting that no bimetallic compounds are formed. The presence of $\text{Fe}_{0.81}\text{Mo}_{1.19}\text{N}_2$ (JCPDS 86-0197), the XRD pattern of which is similar to that of $\text{Mo}_{0.82}\text{N}$, was excluded considering the significant shift observed for the reflection around 49.5° (49.0° for $\text{Fe}_{0.81}\text{Mo}_{1.19}\text{N}_2$).

On the other hand, five consecutive cycles up to 700°C result in the transformation of the Fe–Mo active phase into nitrides. Despite the low intensity of their reflections, the Rietveld analysis of the aged $\text{Fe}_{10}\text{Mo}_{10}/\text{YSZ}$, $\text{Fe}_5\text{Mo}_5/\text{YSZ}$ and $\text{Fe}_5\text{Mo}_5/\text{LSZ}$ evidences the presence of $\text{Mo}_{0.82}\text{N}$ (JCPDS 75-1006) and another phase with the structure of $\text{Fe}_3\text{N}_{1.24}$ [46]. Although the mismatch between the experimental cell parameters of $\text{Mo}_{0.82}\text{N}$ and their theoretical values is negligible, the experimental cell parameters of the $\text{Fe}_3\text{N}_{1.24}$ phase are significantly larger than the expected values. This result indicates that a fraction of Mo is incorporated into the Fe nitride phase, that is better described as $\text{Fe}(\text{Mo})_3\text{N}_{1.24}$ in Table 4. The presence of other iron–molybdenum nitrides, such as $\text{Fe}_{0.81}\text{Mo}_{1.19}\text{N}_2$ or $\text{Fe}_3\text{Mo}_3\text{N}$, can be excluded since their XRD patterns do not agree with the experimental reflections observed. The low intensity of the reflections does not allow a reliable estimation of relative amounts and the exact composition of these phases. Considering the crystallite sizes of the different phases, the values obtained for the supports are very similar to the corresponding values observed after reduction (see Table 3). On the other hand, the crystallite sizes of the various phases containing Fe and/or Mo are larger than the crystallite sizes observed for the highly dispersed Fe–Mo alloys present after reduction at 800°C , evidencing that the deep

sinterization is associated with the decomposition of the alloy and with the formation of the $\text{Mo}_{0.82}\text{N}$ and $\text{Fe}(\text{Mo})_3\text{N}_{1.24}$ phases.

It is well known that nitrides of transition metals, including Fe and Mo, can be formed by reaction of metals or metals oxides with gaseous ammonia [47]. The activity of metal nitrides for ammonia decomposition strongly depends on the nature of the metal. The activity of nanocrystalline Fe in ammonia decomposition was reported to increase as the amount of nitride increased while, as the amount of adsorbed N was high enough to form Fe_4N , the reaction rate significantly decreased [48,49]. Molybdenum nitrides (such as Mo_{16}N_7 , Mo_2N and MoN) demonstrated good ammonia decomposition activities, in forms of powder and films [24,47] or supported on Al_2O_3 [50]. Mixed nitrides, such as $\text{Fe}_3\text{Mo}_3\text{N}$, $\text{Co}_3\text{Mo}_3\text{N}$ and $\text{Ni}_3\text{Mo}_3\text{N}$, exhibited higher activity with respect to Mo_2N [50–52]. The formation of nitrides containing Mo ($\text{Mo}_{0.82}\text{N}$ and $\text{Fe}(\text{Mo})_3\text{N}_{1.24}$) justifies the good stability observed in our supported Fe_5Mo_5 -based catalysts.

4. Conclusions

Active and stable Fe/Mo-based catalysts for H_2 production by NH_3 decomposition were prepared by co-impregnation of the support with $\text{MoO}_2(\text{acac})_2$ and $\text{Fe}(\text{acac})_3$, followed by calcination and activation under H_2 at 800°C . The preparation and activation procedures were optimized in order to obtain nanoparticles of Fe–Mo alloy with a high dispersion on the support. Bimetallic Fe_5Mo_5 -based catalysts demonstrated higher activity than the correspondent monometallic Fe_{10} - and Mo_{10} -based catalysts. While catalysts supported on stabilized zirconias showed similar catalytic activity, a significant improvement in the NH_3 conversion was observed for $\text{Fe}_5\text{Mo}_5/\text{La–Al}_2\text{O}_3$, as a result of improved basicity of the support. All the catalysts investigated demonstrated good

stability under prolonged NH_3 decomposition test at 650°C (120 h). Characterization of the aged samples evidenced the decomposition of the alloy with the consequent formation of $\text{Mo}_{0.82}\text{N}$ and $\text{Fe}(\text{Mo})_3\text{N}_{1.24}$ phases, which still guarantee good activity for NH_3 decomposition. The present study demonstrates the possibility to produce cheap, active and stable catalysts for NH_3 decomposition able to match the requirements for both low temperature (internal combustion engines) and high temperature (ammonia-fed SOFC) applications.

Acknowledgements

Dr. E. Aneaggi and Prof. A. Trovarelli (University of Udine, Italy) are gratefully acknowledged for the access to XRD measurements. Dr. Z. Syrgiannis and Prof. M. Prato (University of Trieste, Italy) is gratefully acknowledged for micro Raman measurements. MEL Chemicals (Manchester, UK) and SASOL (Hamburg, Germany) are acknowledged for kindly providing doped- ZrO_2 and high surface area Al_2O_3 , respectively. Prof. M. Graziani (University of Trieste, Italy) is acknowledged for the helpful discussion. The University of Trieste, ICCOM-CNR, Consortium INSTM and Acta SpA are acknowledged for the financial contribution.

References

- [1] S. Zinoviev, F. Müller-Langer, P. Das, N. Bertero, P. Fornasiero, M. Kaltschmitt, G. Centi, S. Miertus, *ChemSusChem* 3 (2010) 1106–1133.
- [2] I.P. Jain, *International Journal of Hydrogen Energy* 34 (2009) 7368–7378.
- [3] L. Green Jr., *International Journal of Hydrogen Energy* 7 (1982) 355–359.
- [4] M. Ni, M.K.H. Leung, D.Y.C. Leung, *International Journal of Energy Research* 33 (2009) 943–959.
- [5] Y. Lin, R. Ran, Y. Guo, W. Zhou, R. Cai, J. Wang, Z. Shao, *International Journal of Hydrogen Energy* 35 (2010) 2637–2642.
- [6] E. Baniasadi, I. Dincer, *International Journal of Hydrogen Energy* 36 (2011) 11128–11136.
- [7] J.H. Lee, S.I. Lee, O.C. Kwon, *International Journal of Hydrogen Energy* 35 (2010) 11332–11341.
- [8] T. Hollinger, D. Vanderbrook, M. Shciltz, *US2008065136*.
- [9] S.F. Yin, B.Q. Xu, X.P. Zhou, C.T. Au, *Applied Catalysis A: General* 277 (2004) 1–9.
- [10] S.F. Yin, Q.H. Zhang, B.Q. Xu, W.X. Zhu, C.F. Ng, C.T. Au, *Journal of Catalysis* 224 (2004) 384–396.
- [11] S.J. Wang, S.F. Yin, L. Li, B.Q. Xu, C.F. Ng, C.T. Au, *Applied Catalysis B: Environmental* 52 (2004) 287–299.
- [12] S.F. Yin, B.Q. Xu, S.J. Wang, C.F. Ng, C.T. Au, *Catalysis Letters* 96 (2004) 113–116.
- [13] S.F. Yin, B.Q. Xu, C.F. Ng, C.T. Au, *Applied Catalysis B: Environmental* 48 (2004) 237–241.
- [14] S.F. Yin, B.Q. Xu, S.J. Wang, C.T. Au, *Applied Catalysis A: General* 301 (2006) 202–210.
- [15] B. Lorenzut, T. Montini, C.C. Pavel, M. Comotti, F. Vizza, C. Bianchini, P. Fornasiero, *ChemCatChem* 2 (2010) 1096–1196.
- [16] J. Zhang, H.Y. Xu, X.L. Jin, Q.J. Ge, W.Z. Li, *Applied Catalysis A: General* 290 (2005) 87–96.
- [17] W. Zheng, J. Zhang, Q. Ge, H. Xu, W. Li, *Applied Catalysis B: Environmental* 80 (2008) 98–105.
- [18] M. Itoh, M. Masuda, K.I. Machida, *Materials Transactions* 43 (2002) 2763–2767.
- [19] J. Zhang, M. Comotti, F. Schüth, R. Schlögl, D.S. Su, *Chemical Communications* (2007) 1916–1918.
- [20] R. Pelka, P. Glinka, W. Arabczyk, *Materials Science* 26 (2008) 349–356.
- [21] A.H. Lu, J.J. Nitz, M. Comotti, C. Weidenthaler, K. Schlichte, C.W. Lehmann, O. Terasaki, F. Schüth, *Journal of the American Chemical Society* 132 (2010) 14152–14162.
- [22] J.G. Choi, *Journal of Catalysis* 182 (1999) 104–116.
- [23] S.R. Logan, C. Kemball, *Transactions of the Faraday Society* 56 (1960) 144–153.
- [24] H.J. Lee, J.G. Choi, C.W. Colling, M.S. Mudholkar, L.T. Thompson, *Applied Surface Science* 89 (1995) 121–130.
- [25] T. Otremba, N. Frenzel, M. Lerch, T. Ressler, R. Schomäcker, *Applied Catalysis A: General* 392 (2011) 103–110.
- [26] M. Strous, J.J. Heijnen, J.G. Kuenen, M.S.M. Jetten, *Applied Microbiology and Biotechnology* 50 (1998) 589–596.
- [27] T.H. Rod, J.K. Nørskov, *Journal of the American Chemical Society* 122 (2000) 12751–12763.
- [28] R. Di Monte, P. Fornasiero, J. Kaspar, M. Graziani, J.M. Gatica, S. Bernal, A. Gomez-Herrero, *Chemical Communications* (2000) 2167–2168.
- [29] T.V. Choudhary, C. Sivadinarayana, D.W. Goodman, *Catalysis Letters* 72 (2001) 197–201.
- [30] S.M. Karagiozova, *Materials Research Bulletin* 20 (1985) 601–609.
- [31] R. Brown, M.E. Cooper, D.A. Whan, *Applied Catalysis* 3 (1982) 177–186.
- [32] R. Thomas, E.M. van Oers, V.H.J. de Beer, J. Medema, J.A. Moulijn, *Journal of Catalysis* 76 (1982) 241–253.
- [33] K. Koyama, M. Morishita, T. Harada, N. Maekawa, *Metallurgical and Materials Transactions B* 34 (2003) 653–659.
- [34] R. Morales, I. Arvanitidis, D. Sichen, S. Seetharaman, *Metallurgical and Materials Transactions B* 33 (2002) 589–594.
- [35] R. Morales, S. Seetharaman, V. Agarwala, *Journal of Materials Research* 17 (2002) 1954–1959.
- [36] R. Morales, D. Sichen, S. Seetharaman, *Metallurgical and Materials Transactions B* 34 (2003) 661–667.
- [37] R. Morales, *Scandinavian Journal of Metallurgy* 32 (2003) 263–272.
- [38] V.S. Escrivano, E.F. Lopez, M. Panizza, C. Resini, J.M.G. Amores, G. Busca, *Solid State Sciences* 5 (2003) 1369–1376.
- [39] S. Heiroth, R. Frison, J.L.M. Rupp, T. Lippert, E.J. Barthazy Meier, E. Müller Gubler, M. Döbeli, K. Conder, A. Wokaun, L.J. Gauckler, *Solid State Ionics* 191 (2011) 12–23.
- [40] Q. Xu, G. Jia, J. Zhang, Z. Feng, C. Li, *Journal of Physical Chemistry C* 112 (2008) 9387–9393.
- [41] A.M. Beale, S.D.M. Jacques, E. Sacaliuc-Parvulescu, M.G. O'Brien, P. Barnes, B.M. Weckhuysen, *Applied Catalysis A: General* 363 (2009) 143–152.
- [42] G. Magnacca, G. Cerrato, C. Morterra, M. Signoretto, F. Somma, F. Pinna, *Chemistry of Materials* 15 (2003) 675–687.
- [43] S. Xie, E. Iglesia, A.T. Bell, *Journal of Physical Chemistry B* 105 (2001) 5144–5152.
- [44] S. Xie, K. Chen, A.T. Bell, E. Iglesia, *Journal of Physical Chemistry B* 104 (2000) 10059–10068.
- [45] G. Lanzani, K. Laasonen, *International Journal of Hydrogen Energy* 35 (2010) 6571–6577.
- [46] A. Leineweber, H. Jacobs, F. Hüning, H. Lueken, W. Kockelmann, *Journal of Alloys and Compounds* 316 (2001) 21–38.
- [47] R.S. Wise, E.J. Markel, *Journal of Catalysis* 145 (1994) 335–343.
- [48] K. Kielbasa, R. Pelka, W. Arabczyk, *Journal of Physical Chemistry A* 114 (2010) 4531–4534.
- [49] R. Pelka, I. Moszynska, W. Arabczyk, *Catalysis Letters* 128 (2009) 72–76.
- [50] C. Liang, W. Li, Z. Wei, Q. Xin, C. Li, *Industrial and Engineering Chemistry Research* 39 (2000) 3694–3697.
- [51] C.J.H. Jacobsen, *Chemical Communications* (2000) 1057–1058.
- [52] C.S. Lu, X.N. Li, Y.F. Zhu, H.Z. Liu, C.H. Zhou, *Chinese Chemical Letters* 15 (2004) 105–108.